Hyperbolic Regularization of a Pressureless Eulerian Dispersed-Phase Model with One-Group Interfacial Area Transport

B. Kalpaklı* and O. Köken** and M. Akdemir**
Corresponding author: bora@likua.de
* LIKUA UG, DE.
** ROKETSAN Missiles Inc., TR.

Keywords: Eulerian dispersed phase, Pressureless gas dynamics, Hyperbolic regularization, Interfacial area transport (IATE), Break-up/Coalescence.

Abstract

A compact Eulerian dispersed-phase formulation is presented for robust finite-volume simulation of particle-laden solid rocket motor flows. The model targets a common difficulty of pressureless dispersed-phase systems: the loss of strict hyperbolicity and the resulting tendency to form nonphysical concentration spikes under strong compression. To regularize this behavior, a packing-activated friction pressure is introduced. The closure remains inactive in dilute regions but generates a finite, bounded acoustic-like wave speed as the dispersed volume fraction approaches a prescribed packing threshold. This provides a consistent signal-speed estimate for Godunov-type fluxes and is combined with a conservative receiver-side packing limiter to enforce admissible volume fractions.

Particle-size evolution is represented through a one-group interfacial area transport equation, allowing breakup and coalescence effects to modify the local mean diameter without solving a full population balance. The evolving interfacial area feeds back into drag and heat-transfer closures, while all flux and source contributions are linearized using forward-mode automatic differentiation for fully implicit coupling. Numerical demonstrations in axisymmetric and submerged-nozzle solid rocket motor configurations show that the regularized model suppresses pressureless delta-shock formation, maintains stable dispersed-phase transport in strongly compressive regions, and captures physically meaningful size evolution in recirculation and nozzle-acceleration zones.

1. Introduction

Eulerian dispersed-phase modeling is attractive for industrial CFD because it avoids the statistical sampling, parcel-management, and load-balancing difficulties associated with large-scale Lagrangian particle tracking. It also couples naturally to cell-centered finite-volume formulations, implicit residual assembly, and unstructured meshes used in production compressible-flow solvers [1]. These features are especially important in propulsion applications, where the dispersed phase interacts with strong acceleration, compressibility, recirculation, and thermal non-equilibrium over a wide range of local particle residence times.

A persistent difficulty, however, is that many dilute Eulerian dispersed-phase formulations are effectively *pressureless*. In such models, the dispersed momentum equations contain convective transport and interphase source terms, but no intrinsic pressure-like stress that can resist local over-compression. In the one-dimensional face-normal limit, the characteristic speeds of the dispersed subsystem collapse to the dispersed normal velocity. The system is then only weakly hyperbolic, and solutions may become highly sensitive to trajectory crossing, mesh alignment, and the numerical dissipation embedded in the chosen flux function. This mathematical structure is closely related to the concentration and delta-shock behavior known from pressureless-gas dynamics [2, 3].

This degeneracy creates a practical problem for Godunov-type finite-volume solvers. Approximate Riemann solvers require a meaningful estimate of the signal speed across each face. If the dispersed phase has no regularizing wave speed, then a compressive particle field can collapse into very thin, high-density structures before interphase drag or diffusion-like numerical effects can act. Such behavior is undesirable in engineering simulations because it contaminates nonlinear convergence, introduces nonphysical packing fractions, and may force excessively small pseudo-time steps or under-relaxation.

A second challenge is the prediction of particle-size evolution. Standard monodisperse Eulerian models usually prescribe a fixed material diameter or convect a representative diameter passively. This is inexpensive, but it removes the feedback loop between local flow conditions and interphase transfer. Breakup and coalescence alter the projected area density, the drag response time, the heat-transfer area, and the thermal/momentum lag between the particle and carrier phases. A full population balance can represent this physics in greater detail, but it also introduces a high-dimensional internal coordinate and substantial computational cost [4]. For a production solid-rocket-motor workflow, a lower-dimensional closure is therefore desirable.

The present work addresses these two limitations with a compact Eulerian formulation. First, a one-group interfacial area transport equation (IATE) is solved as an additional scalar. The transported interfacial area concentration provides a dynamically evolving mean particle size without requiring a full population balance, following the one-group IATE concept used to evolve interfacial area in two-phase systems [5, 6]. Second, the pressureless dispersed subsystem is regularized by a packing-activated friction pressure. The pressure is inactive in dilute regions, where the model should reduce to pressureless transport, but it activates as the local volume fraction approaches a prescribed packing threshold. In the activated regime, it introduces a finite acoustic-like speed and restores strict hyperbolicity along face normals.

The resulting model has three numerical advantages. It provides a physically motivated wave-speed estimate for robust Riemann-solver fluxes, it prevents unbounded local packing through a conservative receiver-side admissibility limiter, and it remains compatible with fully implicit coupling. All flux and source contributions are differentiated with forward-mode automatic differentiation (AD), giving residual-consistent Jacobians for Newton–Krylov or Newton-like implicit strategies [7].

2. Model Formulation

2.1 Dispersed-phase Variables

The dispersed phase is represented by the dispersed mass concentration

$$\rho_d = \alpha\, \rho_{p,m}(T_d), \tag{1}$$

where α is the dispersed volume fraction and $\rho_{p,m}(T_d)$ is the material density of the condensed phase. This definition separates the amount of dispersed material in a control volume from the intrinsic density of the particle material, which may depend on particle temperature. It also gives a direct relation between the conservative mass variable and the packing constraint, since enforcing $\alpha \le \alpha_{\max}$ is equivalent to enforcing $\rho_d \le \alpha_{\max}\rho_{p,m}(T_d)$.

The conservative transported variables are

$$\{\rho_d,\ \rho_d \boldsymbol{V}_d,\ \rho_d E_d\}\,, \quad \text{and optionally} \quad a_i, \tag{2}$$

where $\boldsymbol{V}_d$ is the dispersed-phase velocity, E_d is the total dispersed specific energy, and a_i is the interfacial area concentration. The variable a_i is not treated merely as a post-processing quantity; it is transported and modified by breakup/coalescence source terms, so it directly affects drag and heat transfer through the local mean diameter.

The primitive state recovered from the conservative variables is therefore

$$\boldsymbol{W}_d = (\rho_d, \boldsymbol{V}_d, T_d, a_i)\,, \tag{3}$$

with a_i omitted when the IATE option is disabled. In the IATE-enabled case, the mean diameter is constrained to remain consistent with both the transported dispersed mass and the transported interfacial area. This consistency is important because an independently transported diameter can become incompatible with the local volume fraction after strong compression or expansion.

2.2 Conservative Transport with Friction Pressure

In conservative form, the dispersed mass and momentum equations are

$$\frac{\partial \rho_d}{\partial t} + \nabla \cdot (\rho_d \boldsymbol{V}_d) = 0, \tag{4}$$

$$\frac{\partial (\rho_d \boldsymbol{V}_d)}{\partial t} + \nabla \cdot (\rho_d \boldsymbol{V}_d \otimes \boldsymbol{V}_d + p_{\mathrm{fr}} \boldsymbol{I}) = \boldsymbol{F}_{dg}. \tag{5}$$

Here $\boldsymbol{F}_{dg}$ denotes the interphase momentum exchange with the carrier gas. The additional stress $p_{\mathrm{fr}}\boldsymbol{I}$ is not a thermodynamic gas pressure. It is a numerical/physical regularizing pressure associated with local dispersed-phase packing. Its role is to provide a finite resistance against over-compression only when the dispersed volume fraction enters a near-packed regime.

For a face with unit normal $\boldsymbol{n}$, the normal convective velocity is

$$u_n = \boldsymbol{V}_d \cdot \boldsymbol{n}. \tag{6}$$

The inviscid normal flux of the mass and momentum subsystem can be written as

$$\boldsymbol{F}_n(\boldsymbol{U}_d) = \begin{bmatrix} \rho_d u_n \\ \rho_d \boldsymbol{V}_d u_n + p_{\mathrm{fr}} \boldsymbol{n} \end{bmatrix}. \tag{7}$$

This form makes the role of p_{fr} explicit: it contributes only to the momentum flux, but through the flux Jacobian it also defines the characteristic wave speed used by approximate Riemann solvers.

An energy equation is also transported for thermal coupling. In the present solver, the energy flux is treated consistently with the selected Godunov flux described in Section 5. When the friction pressure is active, the corresponding pressure-work contribution is included in the dispersed energy flux as needed so that the conservative transport remains compatible with the momentum regularization.

2.3 Interfacial Area Transport and Size Closure

A one-group IATE is solved as [5, 6]

$$\frac{\partial a_i}{\partial t} + \nabla \cdot (a_i \boldsymbol{V}_d) = S_{\mathrm{RC}} + S_{\mathrm{BR}}. \tag{8}$$

The left-hand side transports interfacial area with the dispersed phase. The right-hand side changes the total area concentration due to coalescence and breakup. Coalescence reduces interfacial area by merging particles into larger structures, while breakup increases interfacial area by fragmenting particles into smaller structures. In this one-group formulation, the detailed size distribution is not resolved; instead, the first-order effect of size evolution is represented through the evolution of the area concentration.

For spherical particles, the interfacial area per unit mixture volume is related to the dispersed volume fraction and the representative diameter by

$$a_i = \frac{6\alpha}{d_p} = \frac{6\rho_d}{\rho_{p,m} d_p} \quad \Rightarrow \quad d_p = \frac{6\rho_d}{a_i\, \rho_{p,m}}. \tag{9}$$

This relation is used as the closure between transported mass and mean size. It has two useful consequences. First, particle-size changes feed directly into the projected area density and transfer coefficients.

Second, mass conservation and size evolution remain kinematically compatible: if compression increases ρ_d without a proportional increase in a_i, the representative diameter increases; if breakup increases a_i at nearly fixed ρ_d, the representative diameter decreases.

When IATE is disabled, a constant material diameter is used. This gives the usual monodisperse Eulerian model and is retained as a baseline option. The dynamic IATE option can therefore be compared directly against fixed-size simulations using the same transport, flux, and coupling infrastructure.

2.4 Interphase Momentum and Heat Transfer

Interphase momentum exchange is modeled through a drag source $\boldsymbol{F}_{dg}$ using standard particle-drag correlations. The projected area density is computed consistently with the spherical geometry implied by Eq. (9). For a sphere, the projected area-to-surface-area ratio gives

$$A_p = \frac{a_i}{4}, \tag{10}$$

so the drag response changes automatically when breakup or coalescence modifies a_i. The drag law may therefore be written schematically as

$$\boldsymbol{F}_{dg} = K_d(\rho_g, \mu_g, \boldsymbol{V}_g - \boldsymbol{V}_d, d_p, a_i)\,(\boldsymbol{V}_g - \boldsymbol{V}_d), \tag{11}$$

where K_d contains the projected area density and the selected drag coefficient correlation [8].

Heat transfer is treated analogously. A convective heat-transfer coefficient is evaluated from a Nusselt-number correlation, such as the Ranz–Marshall form, using the local mean diameter obtained from Eq. (9) [9]. The interphase heat source can be written schematically as

$$Q_{dg} = h_g a_i (T_g - T_d), \tag{12}$$

where h_g depends on the local Reynolds and Prandtl numbers. Hence the IATE scalar is coupled to both momentum and thermal relaxation: increasing a_i reduces the representative diameter and increases the available transfer area, while coalescence has the opposite effect.

3. Hyperbolic Regularization of a Pressureless System

3.1 Pressureless Degeneracy

The mathematical issue can be seen from the one-dimensional pressureless mass–momentum subsystem. If $p_{\mathrm{fr}} = 0$ and source terms are neglected for the hyperbolic analysis, the conservative variables $\boldsymbol{U} = (\rho_d, \rho_d u)^T$ satisfy

$$\frac{\partial}{\partial t}\begin{bmatrix}\rho_d \\ \rho_d u\end{bmatrix} + \frac{\partial}{\partial x}\begin{bmatrix}\rho_d u \\ \rho_d u^2\end{bmatrix} = 0. \tag{13}$$

The flux Jacobian has a repeated eigenvalue

$$\lambda_1 = \lambda_2 = u, \tag{14}$$

and, in general, does not provide a complete set of independent characteristic fields. Physically, particles moving along intersecting trajectories have no pressure-like restoring mechanism that would prevent multi-stream compression into very narrow density concentrations. This is the origin of the nonclassical concentration and delta-shock behavior associated with pressureless-gas dynamics [2, 3].

In a finite-volume computation, this degeneracy appears at cell faces. A Riemann solver has to decide how information propagates between the left and right states. If the only available wave speed is the normal velocity itself, then compressive states can be under-dissipated exactly where the volume fraction is approaching its physical limit. This motivates the introduction of a packing-activated pressure term that remains dormant in dilute flow but supplies a finite signal speed when local over-compression becomes possible.

3.2 Packing Activation and Friction Pressure Law

We introduce a friction pressure motivated by frictional–collisional stress closures for dense granular materials and compressible granular–gaseous flow models [10, 11]. The packing fraction is defined as

$$\alpha = \frac{\rho_d}{\rho_{p,m}(T_d)}, \qquad \alpha \le \alpha_{\max}. \tag{15}$$

The closure is activated only above a prescribed threshold α_{fr}. Thus, for $\alpha < \alpha_{\mathrm{fr}}$, the model uses

$$p_{\mathrm{fr}} = 0, \tag{16}$$

and the dilute pressureless limit is recovered. For $\alpha \ge \alpha_{\mathrm{fr}}$, the friction pressure is modeled as

$$p_{\mathrm{fr}} = \varepsilon_{\mathrm{eff}}\, \rho_d^{\gamma_p}. \tag{17}$$

The exponent γ_p controls how rapidly the restoring pressure grows with dispersed mass concentration. A larger value increases the stiffness near packing and therefore strengthens the resistance to further compression.

A direct power-law pressure can be too stiff for an implicit production solver if the induced wave speed becomes much larger than the local particle speed. For this reason, the stiffness is bounded by a velocity-gated coefficient,

$$\varepsilon_{\mathrm{eff}} = \min\left(\varepsilon_0,\ \frac{|\boldsymbol{V}_d|^2}{\gamma_p\, \rho_d^{\gamma_p - 1}\, M_{\min}^2}\right). \tag{18}$$

The upper branch ε_0 gives the nominal packing-pressure strength. The second branch limits the acoustic-like speed generated by the pressure law. The velocity gate also suppresses unphysical pressure build-up in nearly stagnant zones, where a large artificial wave speed would mainly degrade nonlinear convergence rather than improve transport accuracy.

In practice, the activation threshold α_{fr} is chosen below $\alpha_{\max}$. This creates a buffer region in which the regularization begins to act before the packing limit is reached. The pressure law and the packing limiter then play complementary roles: the pressure law gives the hyperbolic subsystem a finite propagation speed, while the limiter enforces the hard admissibility constraint on the face transport.

3.3 Restored Hyperbolicity and Bounded Wave Speed

In packing-activated regions, differentiating Eq. (17) with respect to ρ_d gives the dispersed-phase acoustic-like speed

$$c_d^2 = \frac{\partial p_{\mathrm{fr}}}{\partial \rho_d} = \varepsilon_{\mathrm{eff}} \gamma_p \rho_d^{\gamma_p - 1}. \tag{19}$$

Using the velocity-gated definition of $\varepsilon_{\mathrm{eff}}$ then gives the bound

$$c_d \le \frac{|\boldsymbol{V}_d|}{M_{\min}}. \tag{20}$$

For the one-dimensional normal subsystem with active friction pressure, the characteristic speeds become

$$\lambda_{1,2} = u_n \pm c_d. \tag{21}$$

Thus the subsystem is strictly hyperbolic whenever $c_d > 0$. The regularization is therefore local and selective: it changes the mathematical character of the equations only in the regions where the pressureless formulation is most vulnerable to over-concentration.

The bounded wave speed is important for robustness. A pressure law that restores hyperbolicity but produces arbitrarily large wave speeds would force excessive numerical diffusion and could dominate the physical interphase dynamics. Equation (20) prevents this by tying the regularization speed to the local dispersed-phase velocity scale. The resulting signal speed used in the numerical flux is of the form

$$s_d = |u_n| + c_d, \tag{22}$$

which is large enough to stabilize compressive packed states but bounded enough to avoid turning the dispersed phase into an artificially stiff pseudo-gas.

4. IATE Source Terms: Coalescence and Breakup

The IATE source term is decomposed as

$$S_{\mathrm{RC}} + S_{\mathrm{BR}}, \qquad S_{\mathrm{BR}} = S_{\mathrm{RT}} + S_{\mathrm{TI}} + S_{\mathrm{G}}. \tag{23}$$

Here S_{RC} denotes random-collision or turbulence-induced coalescence, while S_{BR} collects breakup mechanisms. The closures are formulated in terms of smooth algebraic functions wherever possible so that the residual can be differentiated consistently by AD. This is important because discontinuous on/off source activation can produce unstable Jacobians in a fully implicit solver.

4.1 Coalescence Contribution

Turbulence-induced coalescence is represented as a collision-frequency process multiplied by a coalescence efficiency, following common bubble/particle population modeling concepts [12, 13]. In the one-group IATE, coalescence acts as a sink of interfacial area,

$$S_{\mathrm{RC}} < 0, \tag{24}$$

because two particles merging into a larger particle reduce the total surface area per unit volume. The collision frequency increases with local dispersed concentration and turbulent agitation, while the coalescence efficiency accounts for the competition between contact time, film drainage, and surface-tension resistance. The practical effect in the present model is an increase of the representative diameter through Eq. (9).

This coalescence term is particularly important in recirculation or stagnant regions. There, particles can have long residence times and repeated interactions, while the mean convective removal rate is weak. A monodisperse fixed-diameter model cannot represent the resulting growth of the local mean diameter. The IATE formulation captures this effect with only one additional scalar equation.

4.2 Breakup Contributions

Acceleration-driven breakup is represented by an RT-type mechanism. It compares the local particle diameter with a critical length scale associated with the destabilizing acceleration. When d_p exceeds the critical value, breakup is activated and the interfacial area increases. To avoid a non-differentiable switch, the activation is smoothed with a $\tanh(\cdot)$ function of the distance from the critical condition. This preserves a continuous derivative for implicit linearization.

Turbulent-impact breakup represents fragmentation by turbulent eddies and local fluctuating stresses. Its intensity scales with a turbulence-level measure, for example a dissipation proxy obtained from a k–ω turbulence model. A packing limiter proportional to the remaining admissible packing capacity, such as $(\alpha_{\max} - \alpha)$, prevents singular or nonphysical source growth near maximum packing. This is consistent with the philosophy of the transport model: source terms may change size, but they should not drive the dispersed phase outside the admissible volume-fraction range.

Gravity or Eötvös-type breakup is included as an additional large-particle fragmentation mechanism. It activates when the relevant Eötvös-like measure exceeds a critical value and relaxes the interfacial area toward the value associated with a critical stable diameter. This term is mainly useful in regions where body-force or acceleration effects dominate the particle deformation scale.

All breakup terms act as sources of interfacial area,

$$S_{\mathrm{BR}} > 0, \tag{25}$$

thereby decreasing the mean diameter according to Eq. (9). The competition between S_{RC} and S_{BR} determines whether the local dispersed phase evolves toward larger agglomerates or smaller fragments. This competition is central to SRM applications because the local particle response time, heat-transfer rate, and nozzle momentum lag depend strongly on the evolving diameter [14, 15].

5. Numerical Method and Implicit Coupling

The governing equations are discretized using a cell-centered finite-volume method on unstructured meshes. For each control volume Ω_i, the semi-discrete residual has the form

$$\frac{d\boldsymbol{U}_i}{dt}|\Omega_i| + \sum_{f\in\partial\Omega_i} \boldsymbol{F}_f A_f - \boldsymbol{S}_i|\Omega_i| = 0, \tag{26}$$

where $\boldsymbol{F}_f$ is the numerical flux through face f, A_f is the face area, and $\boldsymbol{S}_i$ contains interphase and IATE source terms. The dispersed phase is assembled in the same coupled implicit framework as the carrier phase, so drag, heat transfer, friction pressure, packing limitation, and IATE sources all contribute to the nonlinear residual.

5.1 Godunov-type Fluxes for the Regularized Dispersed-phase

Because the regularized subsystem admits a finite c_d from Eq. (20), standard approximate Riemann solvers can be used for the dispersed conservative variables. The simplest option is a Rusanov or local Lax–Friedrichs flux,

$$\boldsymbol{F}_f^{\mathrm{Rus}} = \frac{1}{2}\left(\boldsymbol{F}_{n,L} + \boldsymbol{F}_{n,R}\right) - \frac{1}{2}s_{\max}\left(\boldsymbol{U}_R - \boldsymbol{U}_L\right), \tag{27}$$

with

$$s_{\max} = \max\left(|u_{n,L}| + c_{d,L}, |u_{n,R}| + c_{d,R}\right). \tag{28}$$

This flux is robust because it applies a scalar dissipation proportional to the largest local signal speed [16, 17]. Its drawback is that it can smear sharp gradients when the same dissipation is applied to all characteristic fields.

AUSM+Up is used as a lower-dissipation alternative. In this formulation, the convective part and the pressure-like part of the flux are split, and the friction pressure enters the pressure-splitting contribution. The reference acoustic speed used by the split flux is based on c_d, so the method remains tied to the regularized dispersed-phase physics rather than to the carrier-gas sound speed [18, 19]. This is important because the dispersed subsystem should not inherit an artificial compressibility scale from the gas phase.

An HLLC-type flux is also supported. The left and right wave estimates are constructed from $u_n \pm c_d$, and the middle-wave correction restores contact-like transport of the dispersed variables [20]. The IATE scalar is advected with the dispersed velocity using the same upwind direction as the dispersed mass flux. This keeps area transport consistent with particle transport and avoids artificial separation between mass concentration and interfacial area.

5.2 Packing-limited Conservative Face Transport

To prevent numerical over-packing, face mass transfer is constrained by receiver-side admissibility. The maximum admissible dispersed mass concentration in a receiving cell is

$$\rho_{d,\max} = \alpha_{\max}\rho_{p,m}(T_d). \tag{29}$$

For a given face flux, the donor and receiver cells are identified from the sign of the dispersed mass flux. If accepting the proposed flux would increase the receiver above $\rho_{d,\max}$, the dispersed flux vector on that face is suppressed or limited. The same logic is applied symmetrically for either flow direction, so the limiter does not introduce a preferred mesh direction.

The limiter is conservative at the face level: the flux removed from one side is not separately added elsewhere; rather, the intercell transfer itself is restricted before it enters either residual. This is preferable to a posteriori clipping of cell values, which can destroy conservation and introduce inconsistent Jacobians. The receiver-side form is also physically intuitive: a donor is allowed to release particles only if the receiver has enough admissible packing capacity.

The friction pressure and the packing limiter are deliberately separate mechanisms. The friction pressure regularizes the hyperbolic transport and supplies the wave speed used by the flux function. The limiter enforces the hard admissible bound. In many cells the pressure regularization prevents the limiter from activating; when extreme compression still occurs, the limiter provides the final bound-preserving safeguard.

5.3 Consistent Jacobians via Automatic Differentiation

All dispersed-phase fluxes and IATE source terms, including smooth activation functions, are linearized using forward-mode AD [7]. For a residual vector $\boldsymbol{R}$ assembled from face fluxes and cell sources, the implicit method requires derivatives of the form

$$\frac{\partial \boldsymbol{R}_i}{\partial \boldsymbol{U}_j}, \tag{30}$$

where $j = i$ gives the cell block and j is a neighbor index for face-coupling blocks. AD is used so that the implemented residual and the implemented Jacobian remain algebraically consistent.

This consistency is particularly valuable for the present model because several mechanisms are strongly coupled and nonlinear: a_i changes d_p, d_p changes drag and heat transfer, ρ_d and T_d determine α, α activates the friction pressure, and the friction pressure changes the numerical wave speed. Hand-derived Jacobians for this chain are error-prone and difficult to maintain. Forward-mode AD provides exact directional derivatives of the implemented expressions, which improves robustness when the model is used with second-order reconstruction and fully implicit coupling.

6. Validation and Solid Rocket Motor (SRM) Applications

The proposed dispersed-phase model is a production-level capability that has been **extensively tested and validated** and is **actively used** in coupled multi-dimensional **solid rocket motor (SRM)** simulations. Internal SRM flows pose severe challenges to pressureless Eulerian formulations due to strong acceleration, shear, recirculation, condensed aluminum-oxide loading, slag accumulation, and local packing tendencies [11, 15, 21].

The **hyperbolic regularization** introduced here (packing-activated friction pressure with bounded wave speed) enables robust Godunov-type fluxes (Rusanov/AUSM+Up/HLLC) in regimes where the pressureless subsystem becomes degenerate. Together with the **receiver-side packing limiter** based on $\rho_{d,\max} = \alpha_{\max}\rho_{p,m}(T_d)$, the model maintains bounded packing fractions and improves nonlinear robustness under fully implicit coupling.

In SRM workflows, the one-group IATE provides efficient mean-size evolution (via Eq. (9)) and feeds back consistently into drag and heat transfer, allows practical breakup/coalescence-driven size dynamics at near-monodisperse Eulerian cost.

6.1 2D Axisymmetric Motor: Numerical Stability and Flux Scheme Evaluation

To evaluate the numerical robustness of the proposed regularized framework under severe compressive geometric constraints, a 2D axisymmetric rocket motor configuration was simulated. Specifically, the test case adopts the well-documented subscale geometry of the ONERA C1x rocket motor [22]. However, since the standard configurations in the literature primarily focus on single-phase gas dynamics, the operating and boundary conditions in this study were specifically adapted to accommodate a dispersed particulate phase. Consequently, this setup is intended as a physically realistic, production-level numerical verification benchmark rather than a direct quantitative comparison with experimental data. The resulting radial flow field serves as a rigorous stress test for Eulerian multi-phase models, as it continuously forces the dispersed phase toward the centerline, inherently triggering severe local packing and numerical singularities.

When utilizing the proposed regularized formulation coupled with either the Rusanov or the AUSM+Up flux schemes, the solution remains perfectly stable and smooth, completely eliminating the formation of non-physical delta shocks. This excellent numerical behavior is directly enabled by the restored strict hyperbolicity along face normals in packed regions, consistent with the need to regularize pressureless/dense-particle transport when density concentrations otherwise form [2, 11]. As the local volume fraction approaches the packing limit, the friction pressure activates a finite, bounded acoustic-like wave speed (c_d), providing the necessary physical restoring force against over-compression [10]. The approximate Riemann solvers (Rusanov and AUSM+Up) leverage this explicit wave speed estimate ($|u_n| + c_d$) to correctly distribute numerical dissipation across cell faces, effectively preventing any localized singular accumulation of the dispersed phase [16, 18, 19].

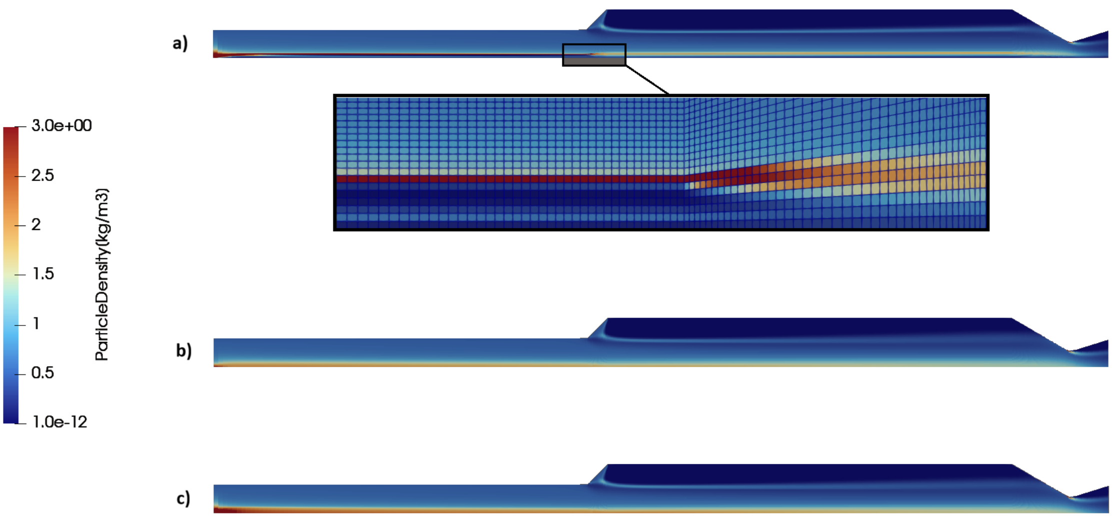

Figure 1: Delta shock generation: (a) unregularized/degenerate formulation, (b) Rusanov flux, and (c) AUSM+Up flux.

Conversely, when running the baseline formulation—denoted as the "unregularized / degenerate" case in the numerical implementation, which lacks this packing-activated regularization—severe delta shocks and non-physical concentration spikes are observed along the symmetry axis. In this unregularized pressureless limit, the characteristic speeds collapse to a single degenerate value equal to the normal velocity, leaving the governing equations without a pressure-like mechanism against over-concentration.

Because the unregularized, pressureless method lacks a proper acoustic-like wave speed estimate, it fails to provide adequate numerical dissipation. Consequently, incoming particle trajectories collapse into very thin, high-density sheets (delta shocks) along the centerline, consistent with the pressureless-gas concentration mechanism described in the literature [2, 3]. This comparison clearly demonstrates that the proposed hyperbolic regularization is a strictly necessary mathematical extension for achieving production-level stability in complex contracting multi-phase flows.

Moreover, as expected, the Rusanov scheme exhibits inherently higher numerical dissipation due to its uniform scalar wave-speed treatment across all characteristic fields [16]. In contrast, the AUSM+Up scheme offers a lower-dissipation alternative that preserves sharper gradients by scaling the numerical diffusion more precisely with the local convective velocity [18].

6.2 Validation: Gas-Particle Flow Over a Backward-Facing Step

To rigorously evaluate the predictive capability of the developed Eulerian multi-phase framework for separating and recirculating flows, a classical single-sided backward-facing step (BFS) benchmark was simulated. The numerical setup is configured to replicate the foundational experimental measurements of Ruck and Makiola [24], alongside the reference two-fluid numerical simulations documented by Senapati and Dash [25]. This benchmark serves as an ideal validation test case for dilute gas-particle formulations, as the sharp geometric expansion induces a strong shear layer and a localized recirculation bubble that intensely segregates the dispersed particulate phase based on aerodynamic drag and particle inertia. To guarantee high numerical stability across the high-shear region without generating spurious oscillations near the step corner, the **Rusanov flux scheme** was employed as the approximate Riemann solver for the interfacial flux evaluations.

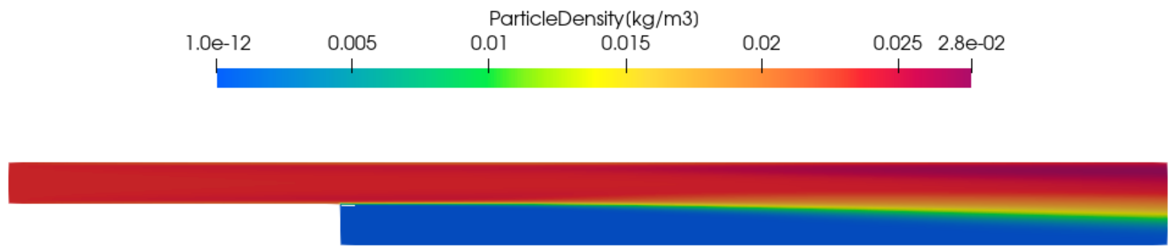

Figure 2: Predicted steady-state particle density (kg/m^3) contour for the single-sided backward-facing step flow configuration.

The macro-scale transport topology of the dispersed phase is illustrated via the steady-state particle density distribution in Fig. 2. Upon passing the sudden expansion corner, the carrier gas phase separates to form a primary recirculation zone along the lower wall. Due to their finite inertia, the incoming solid particles fail to adhere to the sharply turning fluid streamlines, projecting instead into the core shear layer. This inertial mismatch inherently creates a highly distinct, low-density "particle shadow zone" directly behind the step face, where the local particle density drops to the user-specified minimum threshold ($\approx 1.0\times10^{-12}$ kg/m^3, which serves as the default solver floor limit and is fully configurable via the developed GUI of **CMPS**. Further downstream, the particles are dynamically entrained into the lower expanding boundary layer through a combination of convective drag and turbulent dispersion, demonstrating that the regularized Eulerian formulation naturally reproduces the physics of phase segregation without artificial accumulation.

For a quantitative validation, the normalized streamwise particle velocity profiles ($u_{\text{Particle}}/u_{\text{ref}}$) predicted by the proposed framework CMPS are compared against the experimental data of Ruck and Makiola [24] and the reference numerical simulations of Senapati and Dash [25] in Fig. 3. Across all downstream stations (x = 0.225 to 0.425), the CMPS framework successfully captures the qualitative structural evolution of the two-phase jet, clearly distinguishing the high-velocity core from the decelerating shear layer below $y/h = 1.0$.

However, noticeable quantitative discrepancies are observed, particularly within the upper core flow region ($y/h > 1.0$). While both the experimental data and the reference two-fluid simulation exhibit a progressive momentum deficit, with core particle velocities decaying toward $u_{\text{Particle}}/u_{\text{ref}} \approx 0.7 - 0.8$, the CMPS results consistently overpredict the velocity magnitude, maintaining a nearly uniform profile close to unity. This discrepancy is primarily attributed to two modeling limitations: first, the assumption of a simplified, uniform inlet profile that neglects the detailed boundary layer development upstream of the step; and second, the usage of the generic interphase momentum transfer correlation, standard Schiller-Naumann, employed in the current baseline solver and two-way momentum coupling and turbulent dispersion effects in the core stream. Standard drag formulations inherently neglect critical turbulence-induced drag modifications and shear-gradient lift forces, which significantly govern particle redistribution across high-shear interfaces. Customizing the framework with a specialized correlation that accounts for local turbulence intensity or shear-induced lift corrections is expected to drastically improve the predictive accuracy of the velocity profiles within the core region ($y/h > 1.0$).

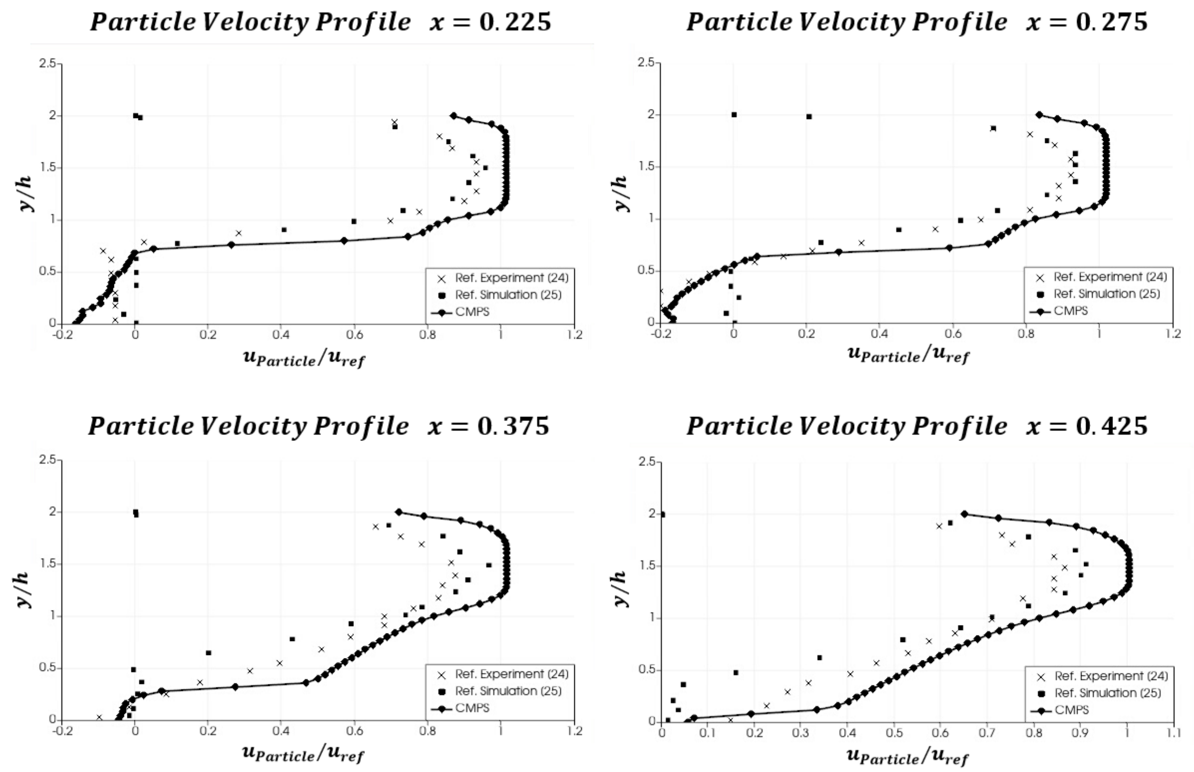

Figure 3: Quantitative comparison of the normalized streamwise particle velocity profiles ($u_{\text{Particle}}/u_{\text{ref}}$) against the experimental data of Ruck and Makiola [24] and the numerical framework of Senapati and Dash [25] at downstream locations $x = 0.225$, $x = 0.275$, $x = 0.375$, and $x = 0.425$.

Furthermore, within the lower shear layer ($y/h < 1.0$), the CMPS profiles exhibit a more rigid, linear velocity transition compared to the smoother, diffusion-driven curves captured by the reference simulation [25]. This indicates that while the regularized formulation coupled with the Rusanov solver ensures exceptional numerical stability across the high-shear expansion zone, the current algebraic or simplified closures for turbulent particle dispersion require further refinement to accurately reproduce complex sub-grid turbulent mixing. Nevertheless, the framework demonstrates a stable, oscillation-free baseline that bounds the physical solution under severe geometric expansion.

6.3 Validation: Compressible Gas-Particle Flow through a Convergent-Divergent Nozzle

To validate the performance of the developed framework in high-speed compressible regimes with strong phase-acceleration gradients, a two-phase flow through a convergent-divergent (de Laval) lüle configuration was investigated. The numerical setup and boundary conditions are modeled based on the benchmark problem proposed by Petitpas and Daniel [26] for dilute compressible mixtures. For this specific test case, the **AUSM+Up flux scheme** was selected to handle the sharp pressure transitions and sonic velocity crossings along the nozzle profile. The validation metrics are extracted along the centerline axis of the nozzle to assess the spatial evolution of both the carrier gas and the accelerated particulate phases.

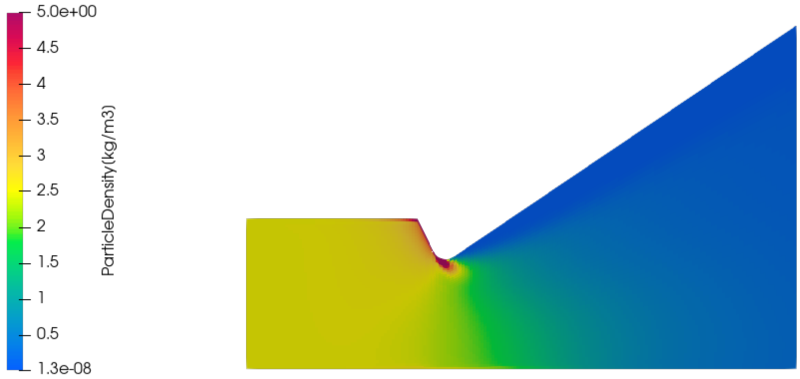

Figure 4: Two-dimensional axisymmetric contour of predicted particle density (kg/m^3) showing the spatial redistribution through the convergent-divergent nozzle.

The overall spatial transport topology is depicted via the two-dimensional particle density contour in Fig. 4. As the multi-phase mixture enters the convergent section, the geometric contraction forces a localized compression of the dispersed phase, leading to a distinct density enhancement near the throat region where values peak up to approximately 55.0 kg/m^3, but the legend is limited to illustrate particle distribution better. Past the throat, as the flow undergoes rapid supersonic expansion into the divergent section, the particle density decreases sharply due to both the expanding volume and the significant convective acceleration of the particles, reaching a minimum near the nozzle exit.

A comprehensive quantitative assessment of the solver accuracy is provided in Fig. 5, which displays the centerline distributions of gas pressure, gas Mach number, particle density, and particle x-velocity against the reference data [26]. The thermodynamic and kinematic states of the carrier gas phase exhibit an exceptional match with the reference solution; the continuous expansion from an inlet pressure of 7.0 MPa down to the outlet conditions, along with the corresponding smooth transition from subsonic conditions to a supersonic Mach number of approximately 2.3, is captured with high fidelity.

For the dispersed particulate phase, the proposed **CMPS** framework tracks the reference curves with strong qualitative and quantitative consistency, though minor physical discrepancies emerge under close inspection. In the particle density profile, the solver correctly predicts the initial density accumulation prior to the throat; however, the localized peak density (≈ 2.6 kg/m^3 at $x \approx 0.6$ m) is slightly underpredicted compared to the discrete points of the reference simulation (≈ 2.8 kg/m^3). This dampening of the peak concentration is indicative of the numerical dissipation introduced by the AUSM+Up scheme coupled with the hyperbolic regularization floor, which acts to slightly diffuse intense localized particle packing. Furthermore, the particle x-velocity profile demonstrates an excellent acceleration trajectory, climbing from 350 m/s to over 1600 m/s. A minor velocity lag is observed at the far-divergent region ($x > 1.6$ m), where the CMPS framework yields a slightly lower exit velocity (≈ 1650 m/s) than Ref. [26] (≈ 1720 m/s). This minor underprediction stems from the highly non-linear nature of the interphase drag law under extreme velocity slip conditions in supersonic expansions. Overall, the tight agreement across

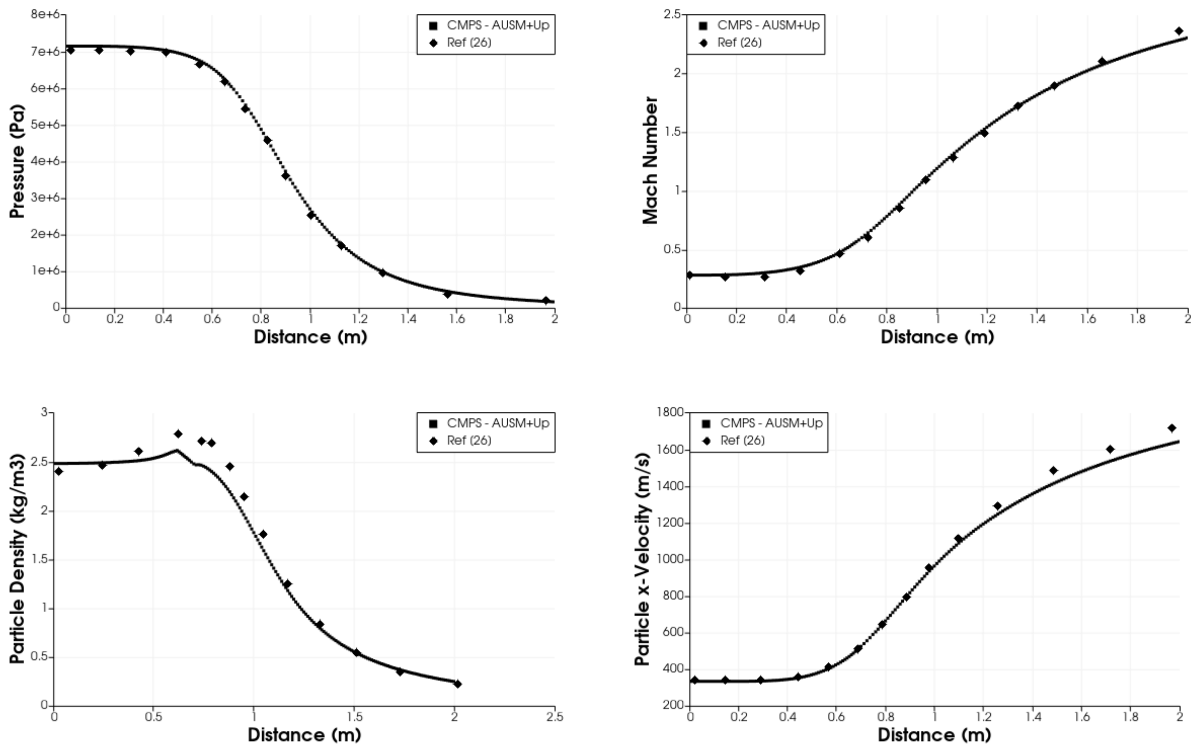

Figure 5: Centerline validation profiles of gas pressure, gas Mach number, particle density, and particle x-velocity compared against the reference compressible formulation of Petitpas and Daniel [26].

all four thermodynamic and kinematic variables successfully confirms the robustness of the framework for coupled, high-speed compressible multi-phase applications.

6.4 2D SRM Thrust Verification and Size Dynamics

To quantify the impact of particle size evolution on motor performance and to validate the predictive capability of the proposed model, a representative 2D Solid Rocket Motor (SRM) configuration operating at a nominal chamber pressure of approximately 6 MPa was simulated. A primary focus of this case study is the assessment of two-phase flow losses—specifically thermal and momentum lag—on the motor's thrust curve under various dispersed-phase assumptions.

The baseline propellant formulation generates a heavy condensed-phase loading, where aluminum oxide (Al_2O_3) particles constitute around 35% of the total mass fraction of the combustion products; such condensed aluminum-oxide products and particle-size effects are central issues in aluminized SRM performance analysis [15]. Five distinct simulation test cases were evaluated and compared against experimental motor thrust data:

- **Pure Gas Phase:** An idealized benchmark assuming 100% gaseous combustion products with no condensed-phase loading, representing the theoretical upper limit of the motor thrust.
- **Monodisperse 5 μm Al_2O_3:** A fixed-size baseline with the IATE framework disabled, assuming no particle breakup or coalescence.
- **Monodisperse 10 μm Al_2O_3:** A fixed-size baseline with the IATE framework disabled.
- **Monodisperse 20 μm Al_2O_3:** A fixed-size baseline with the IATE framework disabled, initialized with a larger diameter that is representative of typical initial aluminum agglomerates at around 6 MPa chamber pressures [15].

- **Dynamic Tracking (IATE Enabled):** The full regularized formulation with the one-group IATE active. The dispersed phase is initialized at the burning surface (inlet) with a representative agglomerate size of 20 μm, while turbulence-induced coalescence and acceleration-driven/turbulent breakup models are fully solved.

The resulting normalized thrust levels (F/F_{ref}) are plotted against the inlet particle size in Fig. 6. The simulations demonstrate the severe limitations of standard monodisperse Eulerian models. For the fixed-size monodisperse runs (represented by the blue curve), a baseline gas flow without particles establishes the reference level. When small 5 μm particles are introduced, a slight non-linear variation in thrust is observed. However, as the prescribed monodisperse particle diameter increases from 5 μm to 20 μm, a sharp performance degradation occurs, with the normalized thrust dropping severely to approximately 95%. This steep penalty is directly attributed to the escalating momentum and thermal lag between the heavy, unyielding dispersed phase and the rapidly accelerating gas phase within the nozzle region—a well-known limitation when particle size evolution and condensed-phase losses are not represented dynamically [15, 21]. The monodisperse 20 μm case, in particular, fails to capture the kinetic recovery of the flow through the nozzle throat, leading to a substantial underprediction of the actual motor performance.

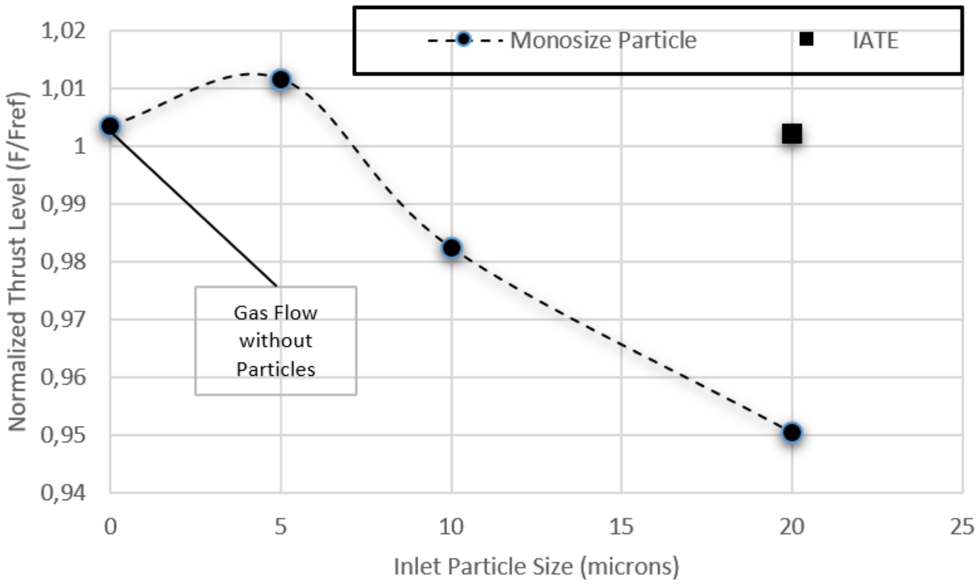

Figure 6: Normalized thrust level (F/F_{ref}) as a function of inlet particle size for fixed monodisperse cases compared against the dynamic tracking (IATE with Coalescence & Break-Up) framework.

In contrast, when the proposed one-group IATE framework is enabled with an initial inlet size of 20 μm, the model dynamically adapts to the high-shear and strong acceleration fields within the core flow and nozzle regions, which leads to superior predictive fidelity. The aerodynamic and turbulent breakup mechanisms, especially at the converging nozzle, rapidly reduce the mean particle diameter in the high-velocity zones, mitigating two-phase flow losses where lag is most critical [13, 14]. Consequently, the dynamic IATE case yields a thrust curve that is in closest numerical agreement with the measured experimental motor thrust level. This highlights that the regularized Eulerian framework delivers production-level accuracy for multi-phase performance predictions at near-monodisperse computational costs.

6.5 2D Submerged Nozzle: Slag Accumulation and Size Dynamics

To demonstrate the robustness, physical consistency, and geometric flexibility of the proposed regularized Eulerian-IATE framework in operational configurations, a qualitative case study involving a 2D submerged nozzle rocket motor geometry was conducted. Submerged nozzles are characterized by complex flow topologies, including severe shear layers, stagnant recirculation zones, and strong geometric turning. This configuration serves as an ideal benchmark for testing the phenomenological capability of multi-phase models in capturing localized particle transport without relying strictly on quantitative validation data.

The model's capacity to resolve sharp spatial concentration variations is illustrated via the particle mass density contours in Fig. 7. The formulation successfully captures the intricate transport driven by secondary flow structures and turbulent dispersion. In the shadow zone directly behind the submerged nozzle nose (the cavity region), the local gas velocity decelerates sharply, creating a massive recirculation bubble. Turbulent dispersion mechanisms effectively drive the dispersed phase into this low-momentum dead zone, leading to a distinct, localized entrapment of particles. This simulated behavior provides a physically consistent representation of the well-known "slag accumulation" or "slag deposition" phenomenon typically encountered in large-scale solid rocket motors [21, 23].

The corresponding size evolution, governed dynamically by the one-group IATE framework, is depicted through the Sauter mean diameter (d_p) contours in Fig. 7. Within the stagnant submerged cavity, the high residence time of the trapped particles, coupled with elevated local turbulent viscosity (μ_t), strongly accelerates the turbulence-induced coalescence rate, consistent with collision-frequency/coalescence-efficiency modeling concepts [12, 13]. Consequently, the model correctly predicts a localized growth in the mean particle diameter within this entrapment zone.

In stark contrast, as the dispersed phase escapes the recirculation zones or enters the main core stream toward the nozzle expansion, it undergoes a completely different physical regime. Upon entering the converging nozzle section and passing through the nozzle throat, the particles experience extreme aerodynamic acceleration and immense fluid shear stress. In these highly convective zones, the IATE breakup source terms—predominantly the acceleration-driven (RT-type) and turbulent-impact breakup mechanisms—instantly dominate over coalescence [14]. This triggers a rapid, sharp fragmentation of the particle phase, resulting in an abrupt reduction of the mean diameter through the throat. This qualitative behavior underlines that the coupling between the regularized pressureless transport and the differentiable IATE source terms remains stable and physically representative even under extreme spatial gradients.

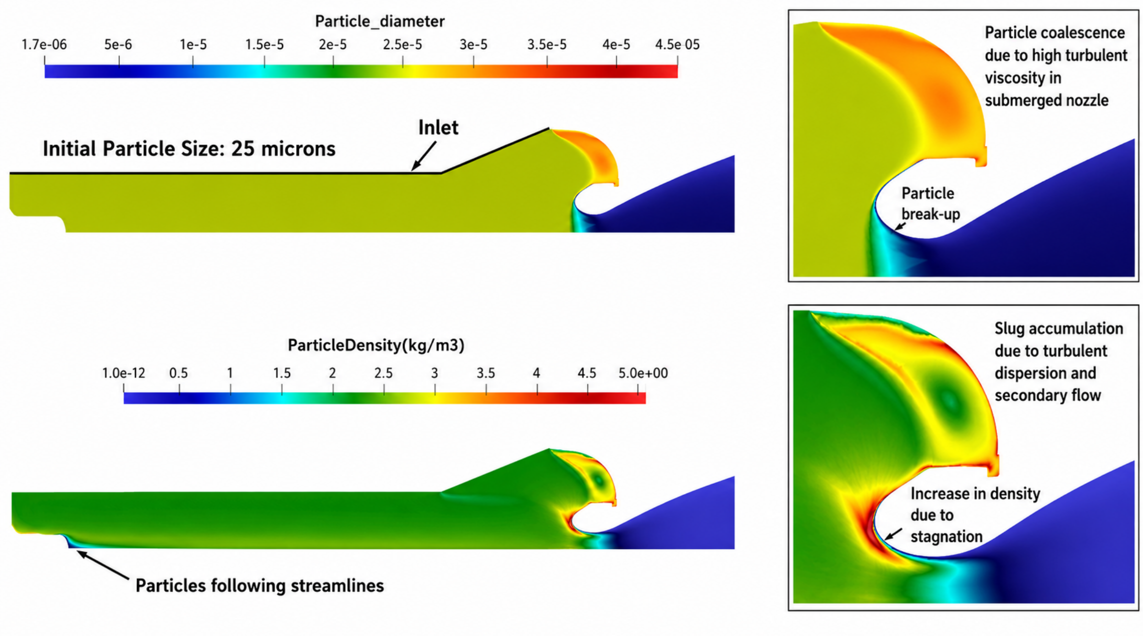

Figure 7: Qualitative flow topology and size dynamics inside a 2D submerged nozzle solid rocket motor configuration, showing particle mass density and Sauter mean diameter (d_p) contours.

7. Conclusions

In this study, a pressureless Eulerian dispersed-phase model has been successfully extended through the integration of a one-group interfacial area transport equation (IATE) and a packing-activated friction-pressure closure. The central mathematical novelty relies on the **hyperbolic regularization** of the pressureless subsystem. By introducing a finite, bounded acoustic-like wave speed within packed zones, the formulation successfully restores strict hyperbolicity along face normals, thereby transforming a mathematically degenerate system into a robust framework compatible with modern Godunov-type approximate Riemann solvers [2, 16, 17, 18, 20]. Supplementing this, a second novelty is introduced via a **packing-limited conservative transport** mechanism. This scheme enforces physical volume-fraction bounds through a symmetric donor/receiver admissibility control based on the receiver-side maximum packing density ($\rho_{d,\max}$), guaranteeing strict mass conservation without numerical over-packing.

The numerical robustness and stability of the developed framework were rigorously evaluated using a 2D axisymmetric stress test based on the subscale geometry of the ONERA C1x rocket motor. In this configuration, where severe radial flow fields continuously force the dispersed phase toward the symmetry axis, the baseline unregularized formulation exhibits a complete mathematical collapse, resulting in non-physical concentration spikes and severe delta shocks along the centerline, consistent with known pressureless-gas delta-shock behavior [2]. Conversely, the proposed regularized framework completely eliminates these singularities, maintaining perfect numerical stability. Furthermore, the evaluation of the flux schemes revealed that while the Rusanov solver provides highly robust and uniform numerical dissipation across all characteristic fields, the AUSM+Up scheme serves as a superior low-dissipation alternative capable of preserving sharper spatial gradients near highly convective zones.

In addition to numerical verification, the phenomenological capability of the coupled model was demonstrated using a production-level 2D submerged nozzle geometry to track localized particle size dynamics. The regularized Eulerian-IATE framework successfully captured intricate multi-phase flow topologies driven by secondary flow structures and turbulent dispersion. In the stagnant cavity behind the nozzle nose, the model accurately predicted the well-known "slag accumulation" phenomenon, capturing the local acceleration of turbulence-induced coalescence due to high particle residence times and elevated turbulent viscosity (μ_t) [12, 21, 23]. Crucially, as the trapped phase escapes into the core stream, the framework dynamically resolves the sudden shift to an aerodynamic breakup regime through the nozzle throat, predicting a sharp and stable reduction in the Sauter mean diameter (d_p).

Ultimately, the proposed mathematical architecture successfully delivers highly descriptive, continuous mean-size dynamics across disparate flow regimes without requiring the staggering computational overhead of a full population balance equation [4, 5]. Coupled with its native support for implicit temporal integration via Automatic Differentiation (AD)-consistent exact Jacobians, this framework provides an exceptionally efficient, stable, and high-fidelity tool for the design and analysis of operational solid rocket propulsion systems [7].

References

[1] D. A. Drew and S. L. Passman, *Theory of Multicomponent Fluids*, Applied Mathematical Sciences, Vol. 135, Springer, New York, 1998.

[2] F. Bouchut, S. Jin, and X. Li, *Numerical approximations of pressureless and isothermal gas dynamics*, SIAM Journal on Numerical Analysis, Vol. 41, No. 1, pp. 135–158, 2003. DOI: 10.1137/S0036142901398040.

[3] C. Chalons, D. Kah, and M. Massot, *Beyond pressureless gas dynamics: quadrature-based velocity moment models*, Communications in Mathematical Sciences, Vol. 10, No. 4, pp. 1241–1272, 2012.

[4] D. Ramkrishna, *Population Balances: Theory and Applications to Particulate Systems in Engineering*, Academic Press, San Diego, 2000.

[5] M. Ishii, S. Kim, and J. Uhle, *Interfacial area transport equation: model development and*

benchmark experiments, International Journal of Heat and Mass Transfer, Vol. 45, No. 15, pp. 3111–3123, 2002.

[6] M. Ishii, X. Sun, S. Kim, and T. Hibiki, *Interfacial area transport equation and implementation into two-fluid model*, Journal of Thermal Science and Engineering Applications, Vol. 1, No. 1, 011005, 2009. DOI: 10.1115/1.3159525.

[7] A. Griewank and A. Walther, *Evaluating Derivatives: Principles and Techniques of Algorithmic Differentiation*, 2nd ed., SIAM, Philadelphia, 2008.

[8] L. Schiller and A. Naumann, *A drag coefficient correlation*, Zeitschrift des Vereins Deutscher Ingenieure, Vol. 77, pp. 318–320, 1933.

[9] W. E. Ranz and W. R. Marshall, *Evaporation from drops, Parts I and II*, Chemical Engineering Progress, Vol. 48, pp. 141–146 and 173–180, 1952.

[10] P. C. Johnson and R. Jackson, *Frictional–collisional constitutive relations for granular materials, with application to plane shearing*, Journal of Fluid Mechanics, Vol. 176, pp. 67–93, 1987. DOI: 10.1017/S0022112087000570.

[11] R. W. Houim and E. S. Oran, *A multiphase model for compressible granular–gaseous flows: formulation and initial tests*, Journal of Fluid Mechanics, Vol. 789, pp. 166–220, 2016. DOI: 10.1017/jfm.2015.728.

[12] H. Luo, *Coalescence, Breakup and Liquid Circulation in Bubble Column Reactors*, Doctoral dissertation, Norwegian Institute of Technology (NTH), Trondheim, 1993.

[13] F. Lehr, M. Millies, and D. Mewes, *Bubble-size distributions and flow fields in bubble columns*, AIChE Journal, Vol. 48, No. 11, pp. 2426–2443, 2002. DOI: 10.1002/aic.690481103.

[14] M. Pilch and C. A. Erdman, *Use of breakup time data and velocity history data to predict the maximum size of stable fragments for acceleration-induced breakup of a liquid drop*, International Journal of Multiphase Flow, Vol. 13, No. 6, pp. 741–757, 1987. DOI: 10.1016/0301-9322(87)90063-2.

[15] M. W. Beckstead, *A summary of aluminum combustion*, RTO/VKI Special Course on Internal Aerodynamics in Solid Rocket Propulsion, RTO-EN-023, Paper 7, 2002.

[16] V. V. Rusanov, *Calculation of interaction of non-steady shock waves with obstacles*, Journal of Computational Mathematics and Mathematical Physics USSR, Vol. 1, pp. 267–279, 1961.

[17] A. Harten, P. D. Lax, and B. van Leer, *On upstream differencing and Godunov-type schemes for hyperbolic conservation laws*, SIAM Review, Vol. 25, No. 1, pp. 35–61, 1983. DOI: 10.1137/1025002.

[18] M.-S. Liou, *A sequel to AUSM, Part II: AUSM+-up for all speeds*, Journal of Computational Physics, Vol. 214, No. 1, pp. 137–170, 2006. DOI: 10.1016/j.jcp.2005.09.020.

[19] R. W. Houim and E. S. Oran, *A technique for computing dense granular compressible flows with shock waves*, arXiv:1312.1290, 2014.

[20] E. F. Toro, M. Spruce, and W. Speares, *Restoration of the contact surface in the HLL-Riemann solver*, Shock Waves, Vol. 4, pp. 25–34, 1994. DOI: 10.1007/BF01414629.

[21] M. Salita, *Deficiencies and requirements in modeling of slag generation in solid rocket motors*, Journal of Propulsion and Power, Vol. 11, No. 1, pp. 10–23, 1995. DOI: 10.2514/3.23835.

[22] F. Vuillot, *Vortex-shedding phenomena in solid rocket motors*, Journal of Propulsion and Power, Vol. 11, No. 4, pp. 626–639, 1995. DOI: 10.2514/3.23888.

[23] B. Toth, M. R. Lema, P. Rambaud, J. Anthoine, and J. Steelant, *Assessment of slag accumulation in solid rocket boosters: summary of the VKI research*, 43rd AIAA/ASME/SAE/ASEE Joint Propulsion Conference & Exhibit, AIAA Paper 2007-5760, 2007.

[24] B. Ruck and B. Makiola, *Particle dispersion in a single sided backward facing step flow*, Particulate Science and Technology, Vol. 14, No. 6, pp. 787-800, 1988.

[25] S. K. Senapati and S. K. Dash, *Dilute gas-particle flow through thin and thick orifice: a computational study through two fluid model*, Particulate Science and Technology, Vol. 38, No. 6, pp. 711-725, 2019.

[26] F. Petitpas and E. Daniel, *Compressible model for dilute flows*, AIAA Journal, Vol. 53, No. 8, pp. 2289–2299, 2015.